



## Simultaneous polarization engineering and selectivity regulation achieved using polymeric carbon nitride for promoting NO<sub>x</sub> photo-oxidation

Zhenyu Wang <sup>a</sup>, Qiuhua Wei <sup>b</sup>, Ning Zhang <sup>a</sup>, Xianjin Shi <sup>a</sup>, Meijuan Chen <sup>c</sup>, Yu Huang <sup>a,\*</sup>, Junji Cao <sup>a,d,\*\*</sup>, Haiwei Li <sup>e</sup>, Wingkei Ho <sup>f</sup>, Shuncheng Lee <sup>g</sup>

<sup>a</sup> Institute of Earth Environment, CAS Center for Excellence in Quaternary Science and Global Change, Chinese Academy of Sciences (CAS), Xi'an 710061, PR China

<sup>b</sup> Department of Disinfection and Control, Chinese PLA Center for Disease Control and Prevention, Beijing 100071, PR China

<sup>c</sup> School of Human Settlements and Civil Engineering, Xi'an Jiaotong University, Xi'an 710049, PR China

<sup>d</sup> Institute of Atmospheric Physics, Chinese Academy of Sciences (CAS), Beijing 100029, PR China

<sup>e</sup> Nanjing University of Information Science and Technology, Nanjing 210044, PR China

<sup>f</sup> Department of Science and Environmental Studies, The Education University of Hong Kong, Hong Kong Special Administrative Region

<sup>g</sup> Department of Civil and Environmental Engineering, The Hong Kong Polytechnic University, Hong Kong Special Administrative Region



### ARTICLE INFO

**Keywords:**  
Polarization  
Selectivity  
Carbon nitride  
Hydroxylation  
NO<sub>x</sub>-removal mechanism

### ABSTRACT

Sluggish charge kinetics and high NO<sub>2</sub> selectivity are still the bottleneck issues that restrict the efficient NO<sub>x</sub> photo-oxidation and removal using polymeric carbon nitride (PCN). Herein, approximately 2 times higher NO<sub>x</sub>-removal performance and almost complete NO<sub>2</sub>-inhibition can be synchronously achieved by maximizing the versatility of the coupled hydroxyl groups. The experimental and computational results reveal the roles of different types of coupled-hydroxyl groups in PCN in the enhancement of photocatalytic activity in terms of NO<sub>x</sub> removal and product selectivity. The spontaneous polarization effect caused by the introduction of the structural hydroxyl into the C<sub>6</sub>N<sub>7</sub> framework accounts for the improved separation efficiency of the carriers. The mediated role of product selectivity was attributed to the process of surface hydroxyl grafting. Different conversion pathways for NO<sub>x</sub> photo-oxidation over pristine and hydroxylated-PCN were proposed. These findings provide molecular-level insight into the multiple roles of the coupled hydroxyls and can help design efficient NO<sub>x</sub>-removal photocatalysts.

### 1. Introduction

Nitrogen oxides (NO<sub>x</sub> = NO+NO<sub>2</sub>) are categorized as air pollutants that harm the environment because they contribute to haze-and ozone formation [1,2]. Traditional NO<sub>x</sub> elimination technologies are suitable for the removal of NO<sub>x</sub> emitted from the source [3], but ineffective to eliminate NO<sub>x</sub> at ambient concentration levels [4,5]. Photocatalysis has attracted immense attention as an alternative as it can be used for removing low concentrations of NO<sub>x</sub>. The catalysts can utilize abundant solar energy and function under ambient working conditions [4–8]. Photo-generated active species can oxidize gas-phase NO<sub>x</sub> to particulate-phase nitrate/nitrite, which not only purifies the air but also functions as a source of nitrogen for microorganisms [9,10]. Polymeric carbon nitride (PCN), a covalent polymer, belongs to the class of

metal-free and organic semiconductor photocatalysts. It has drawn increasing attention as it is characterized by unique chemical composition, crystal structure, and band structure. It exhibits superior biocompatibility, structural adjustability, and visible-light response [11–15]. Since 2013, PCN and PCN-based photocatalysts have been continually used in the field of photocatalytic NO<sub>x</sub>-removal to realize environmental remediation and address academic curiosity [5,13,16–19].

However, according to previous studies (Table S1), the efficient removal of NO<sub>x</sub> using PCN or PCN-based photocatalysts remains challenging due to high NO<sub>2</sub> selectivity and uncontrollable NO<sub>2</sub> conversion pathway. Previous studies have indicated that different active species (primarily involving superoxide, hole, and hydroxyl) oxidize NO<sub>x</sub> in different pathways (NO + •O<sub>2</sub> → NO<sub>2</sub>/•O-NO<sub>2</sub> (1); NO/NO<sub>2</sub> + O<sub>2</sub><sup>-</sup>(lattice)(hole) → NO<sub>2</sub>/•O-NO<sub>2</sub> (2); NO/NO<sub>2</sub> + •OH → HNO<sub>2</sub>/HNO<sub>3</sub> (3),

\* Corresponding author.

\*\* Corresponding author at: Institute of Earth Environment, CAS Center for Excellence in Quaternary Science and Global Change, Chinese Academy of Sciences (CAS), Xi'an 710061, PR China.

E-mail addresses: [huangyu@ieecas.cn](mailto:huangyu@ieecas.cn) (Y. Huang), [jjcao@mail.iap.ac.cn](mailto:jjcao@mail.iap.ac.cn) (J. Cao).

respectively [9,20,21]. In a previous study, experiment and calculation results indicate that surface hydroxyl groups present on TiO<sub>2</sub> contributed to NO<sub>2</sub> adsorption and transformation, leading to the inhibition of NO<sub>2</sub> emission [22]. The photocatalytic reaction over pristine PCN cannot directly produce hydroxyl radicals because its valence-band edges potential (approximately in the range of 1.2–1.6 V) is lower than that of H<sub>2</sub>O•OH (2.37 V) [13,19]. Moreover, during gas-solid reactions, the multistep photoreduction of O<sub>2</sub> can generate few hydroxyl radicals as water molecules rarely spontaneously ionize in the vapor state to produce protons under ambient working conditions. In addition, without lattice O in PCN, the NO<sub>2</sub> emission path represented by equation (2) can be ignored, and inhibiting the generation of NO<sub>2</sub> through the creation of oxygen vacancies cannot be achieved. These limitations result in high NO<sub>2</sub> selectivity (the average value is approximately 50%, Table S1) in the presence of pristine PCN, and PCN-based photocatalysts. Therefore, it is important to develop an effective strategy to introduce •OH in the NO<sub>x</sub>-removal process to steer the NO<sub>x</sub> conversion pathway when PCN and PCN-based catalysts are used as photocatalysts.

How can •OH be introduced over PCN? Ye and co-workers reported that surface-alkalinized photocatalysts (e.g., WO<sub>3</sub> and SrTiO<sub>3</sub>) could be used to introduce •OH by grafting hydroxyl groups [23,24]. In light of this, Li et al. introduced KCl and NaOH/NH<sub>4</sub>Cl during the polymerization of melamine to prepare alkalinized PCN, which can produce •OH. Simultaneously, they found that the potential of the valence-band edge of PCN thermodynamically disfavors the oxidation of OH<sup>−</sup> (approximately 1.98 V vs. normal hydrogen electrode). The generation of •OH was attributable to the conversion of grafted hydroxyl groups since the steady chemisorption of the reactant over the catalyst reduced the thermodynamic requirement [25–27]. To date, the hydroxylation of PCN has been realized through alkaline precursor calcination, solvothermal treatment, and alkaline liquid impregnation. However, the effects of the OH groups generated during the hydroxylation of PCN on NO<sub>x</sub>-removal and product selectivity remain unknown. Sano et al. and Nie et al. prepared hydroxyl-grafted PCN by melamine (or dicyandiamide) calcination followed by 18 h alkaline hydrothermal treatment. The researchers attributed the enhanced NO-removal activity to the increased specific surface area [16,28]. Recently, Gu et al. reported carbon vacancies and hydroxyl-co-modified PCN to improve the NO removal performance. The grafted OH groups and carbon vacancies help synergistically accelerate charge carrier separation. The effects of grafted OH on the regulation of product selectivity and NO<sub>x</sub> removal remain unanswered [29]. In addition, the influence of hydroxyl group location on the photocatalytic activity during NO<sub>x</sub> oxidation over PCN was not understood clearly.

In this study, we synthesized hydroxylated PCN through short-time alkaline hydrothermal treatment and alkaline liquid impregnation methods. The photocatalytic performances of as-prepared samples were evaluated in terms of NO<sub>(x)</sub> removal ratio and NO<sub>2</sub> selectivity. The roles of different hydroxyl groups in photocatalytic activity and product selectivity were systematically investigated by experiments and theoretical calculations. This study reveals hydroxyl-mediated reaction pathways in which NO<sub>x</sub> oxidation follows over PCN for the first time. This contribution offers a novel way to improve the photocatalytic activity and product selectivity of PCN simultaneously.

## 2. Experimental section

### 2.1. Synthesis of hydroxyl decorated polymeric carbon nitride

Urea powder (10 g) was put into a 50-mL crucible with a cover. It was heated to a temperature of 550 °C for 3 h at a heating rate of 5 °C/min. The resulting material was designated as PCN. Following this, 0.75 g of PCN was mixed with a solution of NaOH (from 0.01 M to 0.25 M; 75 mL) under conditions of vigorous stirring (time: 30 min). The formed suspension was transferred into a 100-mL Teflon-lined autoclave and

heated from 80° to 130°C for different times (from 1 h to 9 h). The product was filtered and washed with deionized water and absolute ethanol thrice. Subsequently, the sample was dried at 80 °C for 20 h. The obtained sample after treating with 0.1 M NaOH and heating at 90 °C for 5 h was chosen as the representative sample (according to the result of elemental analysis, this sample was labeled as C<sub>3</sub>N<sub>4.47</sub>H<sub>3.76</sub>O<sub>1.15</sub>) because of the optimal photocatalytic performance (experimental results of variable optimization were shown in Fig. S1 and Table S2). The same procedure was followed to synthesize another sample labeled C<sub>3</sub>N<sub>4.42</sub>H<sub>2.80</sub>O<sub>0.92</sub> according to the result of elemental analysis. The characteristics of the two samples were compared. In this case, instead of the alkaline hydrothermal method, the impregnation treatment method (0.1 M NaOH; 75 mL) was followed for 5 h at room temperature.

### 2.2. Characterization

The phase structure was recorded by the X-ray diffraction (XRD) measurements under conditions of Cu K $\alpha$  radiation (X'Pert PRO, PANalytical, UK). The functional groups were identified by the Fourier transform infrared (FT-IR) measurements (VERTEX 70, Bruker, Germany). The elements in the samples were recorded using an Elementar Vario EL instrument (Vario EL III, Germany, the detection limit is 0.015%, standard deviation < 0.1% abs). The surface bonding element was analyzed by X-ray photoelectron spectroscopy (XPS, ESCALAB 250, Thermo Fisher, USA). All binding energies were calibrated against the C 1 s peak (284.8 eV, surface-adventitious carbon). The morphology was examined by the field-emission scanning electron microscope (SEM, TESCAN MAIA3, Czech). The specific surface area was analyzed on a nitrogen-adsorption analyzer (ASAP 2460, Micromeritics, USA, pretreatment temperature: 250 °C). The light absorption capacity was evaluated using a UV-visible spectrophotometer (Varian Cary 100 Scan, Agilent, Australia). The surface products produced after the photocatalytic reaction were detected using the ion chromatography technique. A Dionex-600 Ion Chromatograph (IC, Dionex Inc., Sunnyvale, CA, USA) fitted with an IonPac AS14A column was used for the studies. The concentrations of the photoinduced oxygen species were detected using an electron spin resonance (ESR) spectrometer (ELEXSYS E500, Bruker, Germany). The separation and migration behaviors of the photo-generated charges were evaluated using an electrochemical workstation (Parstat 4000, USA) fitted with a three-electrode cell configuration, a fluorescence spectrophotometer (FLS980, Edinburgh Instruments, Britain), and a kelvin probe force microscope (KPFM, Multimode 8, Bruker, Germany). The surface functional groups changed during the process of photocatalytic NO<sub>x</sub> oxidation. The change was recorded using the in-situ diffuse reflectance infrared Fourier-transform spectroscopy (DRIFTS) technique. An FT-IR spectrometer equipped with a high-sensitivity mercury cadmium telluride (MCT) detector and an in-situ diffuse reflectance cell system (Harrick, USA) was used to record the changes.

### 2.3. Density functional theory (DFT) parameters

Calculations for structure optimization and reaction mechanisms were carried out using the DFT technique. The Perdew–Burke–Ernzerhof (PBE) generalized gradient approximation and norm-conserving pseudo-potentials implemented in the Vienna ab initio simulation package (VASP) code were used for the calculations [30–32]. The cutoff energy of the plane-wave basis set was 520 eV. During the process of geometry optimization, the convergence criterion was set to 10<sup>−5</sup> eV/atom for energy and 0.03 eV/Å for force. The K point mesh was a gamma point centered grid (1 × 1 × 1 for isolated molecules and 3 × 3 × 1 for crystals and surfaces). The PCN (001) surface was built from the optimized orthorhombic PCN bulk unit cell (lattice parameters: a = 16.868 Å, b = 12.758 Å, and c = 3.59 Å). The surface slab was built by constructing a 15 Å vacuum. The possibilities of OH graft sites were examined to build the C<sub>3</sub>N<sub>4.47</sub>H<sub>3.76</sub>O<sub>1.15</sub> and C<sub>3</sub>N<sub>4.42</sub>H<sub>2.80</sub>O<sub>0.92</sub> surface models. The number of electrons in the target atoms was calculated

following the process of Bader charge analyses [33]. The transition state was searched for in the minimum energy pathway following the climbing image nudged elastic-band (CI-NEB) method, and its validity was verified following the process of vibrational frequency analysis [34].

#### 2.4. Photocatalytic activity experiments

A vitreous culture dish (diameter: 10.0 cm) containing 0.1 g of the as-prepared sample was placed in the rectangular reactor (30 cm × 15 cm × 10 cm, 4.5 L). The initial NO gas was supplied from a compressed gas cylinder (48 ppm N<sub>2</sub> balance) and diluted to 400 ppb using a zero-air generator. The flow rate was set at 3 L/min (Model 1001, Sabio Instruments Inc., Georgetown, TX, USA). A 300-W commercial Xe arc lamp (Cel-hxf300, China Education AuLight, China) fitted with a UV-cutoff filter was placed vertically outside the reactor. The schematic diagram of the experimental set-up system described above is shown in Fig. S2. The optical power at the sample surface was recorded by the optical power meter (PM100D, Thorlabs, USA) and the corresponding optical power density was 13.88 mW/cm<sup>2</sup>. The temperature evolutions over the catalysts during visible-light irradiation were tracked using a thermocouple thermometer (UNI-T, UT320D, range: 0 °C–1000 °C, precision: ± 0.5% rdg + 1 °C, China). The change in the NO<sub>x</sub> concentrations before and after lighting was recorded online on a Model 42c chemiluminescence NO analyzer (Thermo Environmental Instruments Inc., Franklin, MA, USA). The removal ratio ( $\eta$ ) for NO<sub>(x)</sub>, NO<sub>2</sub> selectivity, electric energy per order (E<sub>EO</sub>), and the apparent quantum yield (AQY) were calculated and their details were provided in the supporting information.

### 3. Results and discussion

#### 3.1. Structural characterization of hydroxylated-PCN

The phase structures of the representative samples were investigated using the XRD technique. As presented in Fig. 1a, the XRD patterns recorded for PCN and C<sub>3</sub>N<sub>4.42</sub>H<sub>2.80</sub>O<sub>0.92</sub> exhibit two typical diffraction peaks at approximately 13.2° and 27.3°, respectively. The former is assigned to the intralayer long-range-ordered tri-s-triazine (C<sub>6</sub>N<sub>7</sub>) units (100), and the latter is assigned to the periodic stacking (002) of layers along the c-axis [11]. However, the (100) peak of C<sub>3</sub>N<sub>4.47</sub>H<sub>3.76</sub>O<sub>1.15</sub> disappears, suggesting the distortion of the periodic structure of the C<sub>6</sub>N<sub>7</sub> framework following alkaline hydrothermal treatment. This result was further verified by analyzing the FT-IR spectral profiles (Fig. S3, the detailed descriptions are provided in the supporting information). The above results and analyses suggest that the distortion of the C<sub>6</sub>N<sub>7</sub> units present in C<sub>3</sub>N<sub>4.47</sub>H<sub>3.76</sub>O<sub>1.15</sub> could be attributed to the introduction of the OH group into the C<sub>6</sub>N<sub>7</sub> framework following the process of alkaline hydrothermal treatment, and OH groups could be grafted onto the surface of the C<sub>6</sub>N<sub>7</sub> units following alkaline solution impregnation [25,35].

The elements in the samples were analyzed, and XPS profiles of the samples were recorded to further identify the changes in the chemical composition of the representative samples. The results of the elemental analysis are presented in Table S3. The composition of PCN was C<sub>3</sub>N<sub>4.42</sub>H<sub>2.41</sub>O<sub>0.56</sub>, indicating the presence of primary (–NH<sub>2</sub>) and secondary amino groups (–NH–). Therefore, the structural model of the prepared PCN was closer to the model of the 1-dimensional chains of the NH-bridged tri-s-triazine units ([C<sub>6</sub>N<sub>7</sub>(NH<sub>2</sub>)(NH)]<sub>n</sub>, Fig. S4a) than the models of the perfect tri-s-triazine units (Fig. S4b) [16,36]. The compositions of the hydrothermal sample and impregnated sample were C<sub>3</sub>N<sub>4.47</sub>H<sub>3.76</sub>O<sub>1.15</sub> and C<sub>3</sub>N<sub>4.42</sub>H<sub>2.80</sub>O<sub>0.92</sub>, respectively. The C/N ratios were almost constant (unlike the case observed in PCN), while the contents of H and O atoms increased approximately in the ratios of 2:1 and 1:1, respectively. The XPS profiles were recorded to further

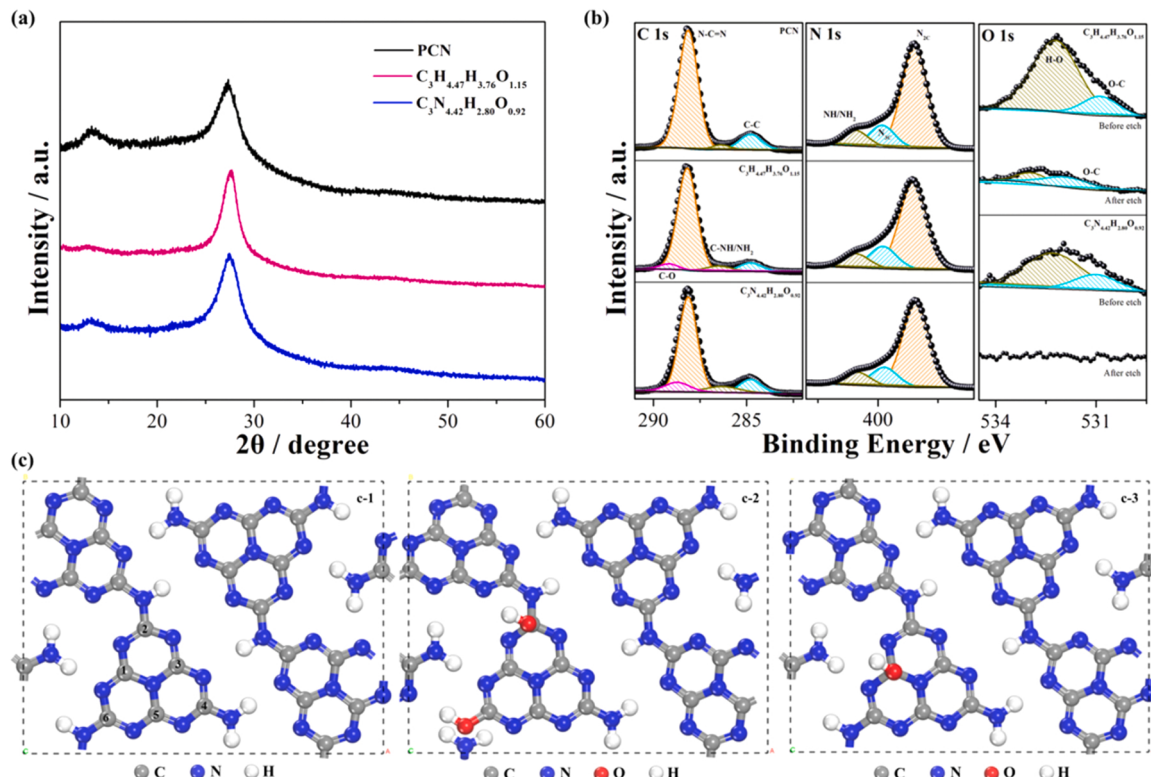


**Fig. 1.** (a) XRD patterns and (b) XPS profiles recorded for PCN, C<sub>3</sub>N<sub>4.47</sub>H<sub>3.76</sub>O<sub>1.15</sub>, and C<sub>3</sub>N<sub>4.42</sub>H<sub>2.80</sub>O<sub>0.92</sub>. (c) (001) crystal face of PCN (c-1), C<sub>3</sub>N<sub>4.47</sub>H<sub>3.76</sub>O<sub>1.15</sub> (c-2), and C<sub>3</sub>N<sub>4.42</sub>H<sub>2.80</sub>O<sub>0.92</sub> (c-3) determined by the process of structural optimization.

investigate the surface elemental compositions and states. The profiles recorded for PCN reveal the presence of three C 1 s peaks at 288.1, 286.4, and 284.8 eV, corresponding to the N-C≡N, C-NH/NH<sub>2</sub>, and adventitious C-C bonds, respectively (Fig. 1b) [37]. As for C<sub>3</sub>N<sub>4.42</sub>H<sub>2.80</sub>O<sub>0.92</sub>, the peak corresponding to the C-O bond can be detected at 288.7 eV [29]. The binding energy of C-O bond drift was observed in C<sub>3</sub>N<sub>4.47</sub>H<sub>3.76</sub>O<sub>1.15</sub>, indicating that the coordination environment of the C-O band was different from that present in C<sub>3</sub>N<sub>4.42</sub>H<sub>2.80</sub>O<sub>0.92</sub>. The N 1 s peaks of all the as-prepared samples were observed at approximately 398.5, 399.8, and 400.9 eV, corresponding to the bi-coordinated (N<sub>2</sub><sub>C</sub>) and tri-coordinated (N<sub>3</sub><sub>C</sub>) nitrogen atoms and NH<sub>x</sub> groups, respectively [37]. The O 1 s XPS profiles recorded for PCN only contain one component at approximately 532.3 eV, which was assigned to the O-H band present in the adsorbed H<sub>2</sub>O unit (Fig. S5) [26]. As for C<sub>3</sub>N<sub>4.47</sub>H<sub>3.76</sub>O<sub>1.15</sub> and C<sub>3</sub>N<sub>4.42</sub>H<sub>2.80</sub>O<sub>0.92</sub>, except for the adsorbed H<sub>2</sub>O, the O-C band peaks (at around 531.0 eV) could be detected [26]. Following the process of Ar<sup>+</sup> etching over 30 s (etching depth: 10 nm), the peaks at approximately 531.0 eV (in the profiles recorded for C<sub>3</sub>N<sub>4.47</sub>H<sub>3.76</sub>O<sub>1.15</sub> and C<sub>3</sub>N<sub>4.42</sub>H<sub>2.80</sub>O<sub>0.92</sub>) disappeared, indicating that the OH groups could be grafted onto the surface of PCN following the process of alkaline solution impregnation. However, the O-C band peak at 531.9 eV could be detected in the O 1 s peak profile of C<sub>3</sub>N<sub>4.47</sub>H<sub>3.76</sub>O<sub>1.15</sub> following etching. This indicated that the OH group could be introduced into the C<sub>6</sub>N<sub>7</sub> framework following alkaline hydrothermal treatment [25,26]. The above results and analyses suggest that alkaline hydrothermal treatment can break the C-NH-C bridge in PCN, resulting in the formation of C-OH and H<sub>2</sub>N-C termini via hydrolysis (Fig. S6). The process of alkaline solution impregnation can only be used to graft the OH group at the surface C-site. The molecular structures of PCN, C<sub>3</sub>N<sub>4.47</sub>H<sub>3.76</sub>O<sub>1.15</sub>, and C<sub>3</sub>N<sub>4.42</sub>H<sub>2.80</sub>O<sub>0.92</sub> were proposed, and these have been schematically shown in Fig. S7.

The density functional theory (DFT) technique was used to build the surface models of PCN, C<sub>3</sub>N<sub>4.47</sub>H<sub>3.76</sub>O<sub>1.15</sub>, and C<sub>3</sub>N<sub>4.42</sub>H<sub>2.80</sub>O<sub>0.92</sub>. The model of the 1-dimensional chains of the NH-bridged tri-s-triazine units of PCN was primarily built and optimized, as shown in Fig. S8. Following this, the (001) lattice plane was cleaved, and the optimized surface slab model is shown in Figs. 1(c-1). In this model, a tri-s-triazine unit contains six carbon atoms. Therefore, six possibilities of surface-OH graft sites were examined (Fig. S9), and the total energies of all the modes were compared (Table S4). The results indicate that the surface OH groups are most easily grafted at the C1 site. The surface model of C<sub>3</sub>N<sub>4.42</sub>H<sub>2.80</sub>O<sub>0.92</sub> is shown in Fig. 1(c-3). C<sub>3</sub>N<sub>4.47</sub>H<sub>3.76</sub>O<sub>1.15</sub> was endowed with the C-OH and H<sub>2</sub>N-C termini, and this could be attributed to the hydrolysis during alkaline hydrothermal treatment (Fig. S6). Therefore, five possibilities of surface-OH graft C-sites were examined (Fig. S10), and the total energies of all the modes were calculated and listed (Table S4). The results indicate that it is easiest to graft the surface OH groups at the C2 site in C<sub>3</sub>N<sub>4.47</sub>H<sub>3.76</sub>O<sub>1.15</sub>. The model is presented in Fig. 1c (c-2).

The morphologies of the representative samples were examined using the SEM technique. As presented in Fig. S11, all the samples exhibited similar microstructural morphology. The samples were irregularly curved and consisted of stacked layers. The layer-stacking degree of C<sub>3</sub>N<sub>4.47</sub>H<sub>3.76</sub>O<sub>1.15</sub> was denser than that of others. Nitrogen adsorption reveals that the specific surface areas of PCN, C<sub>3</sub>N<sub>4.47</sub>H<sub>3.76</sub>O<sub>1.15</sub>, and C<sub>3</sub>N<sub>4.42</sub>H<sub>2.80</sub>O<sub>0.92</sub> were 77 m<sup>2</sup>/g, 41 m<sup>2</sup>/g, and 63 m<sup>2</sup>/g, respectively. The significant decrease in the specific surface area of C<sub>3</sub>N<sub>4.47</sub>H<sub>3.76</sub>O<sub>1.15</sub> was attributed to the self-decomposition of the fluffy thin-layer structure during the process of hydrothermal treatment [38]. The reduced specific surface area is not conducive to the enhancement of the NO<sub>x</sub>-removal activity.

### 3.2. C<sub>3</sub>N<sub>4.47</sub>H<sub>3.76</sub>O<sub>1.15</sub> could achieve 2 times higher NO<sub>x</sub> removal ratios compared to PCN, and almost complete NO<sub>2</sub> inhibition

The photocatalytic oxidation of NO under visible light irradiation

was examined using the representative samples in a continuous reactor to assess the contribution of the grafted hydroxyl groups on the process of improvement of photocatalytic efficiency. As shown in Fig. 2a, the NO-removal ratios ( $\eta$ ) over PCN, C<sub>3</sub>N<sub>4.47</sub>H<sub>3.76</sub>O<sub>1.15</sub>, and C<sub>3</sub>N<sub>4.42</sub>H<sub>2.80</sub>O<sub>0.92</sub> are 23.2%, 30.4%, and 26.7%, respectively. The changes in the NO<sub>2</sub> concentration occurring during the process of photocatalytic NO oxidation in the presence of the representative samples were simultaneously monitored. The growth rate was subsequently calculated. As shown in Fig. 2b, the production of NO<sub>2</sub> in the presence of PCN increases with an increase in the reaction. The slope of linear fitting (Table S5) was 1.037. The corresponding values for C<sub>3</sub>N<sub>4.47</sub>H<sub>3.76</sub>O<sub>1.15</sub> and C<sub>3</sub>N<sub>4.42</sub>H<sub>2.80</sub>O<sub>0.92</sub> were -0.004 and 0.340, respectively, indicating that the introduction of the hydroxyl groups effectively inhibited NO<sub>2</sub> emission. In addition, the NO-removal ratio and production of NO<sub>2</sub> in the presence of PCN remained stable in the time range of 17–21 min. This indicated that the reaction reaches a dynamic equilibrium under these conditions. It was also observed that the production of NO<sub>2</sub> (over PCN) gradually increased after 21 min, indicating the occurrence of NO<sub>2</sub> emission in another route. The NO<sub>2</sub> selectivity and NO<sub>x</sub>-removal ratios of the representative samples were calculated, and the results were summarized (Fig. 2c). The C<sub>3</sub>N<sub>4.47</sub>H<sub>3.76</sub>O<sub>1.15</sub> samples could achieve approximately 2 and 1.2 times higher NO<sub>x</sub>-removal ratios compared to the pristine PCN and C<sub>3</sub>N<sub>4.42</sub>H<sub>2.80</sub>O<sub>0.92</sub>, respectively. This sample also exhibited almost complete NO<sub>2</sub> inhibition. What's more, we tracked the temperature evolutions in the reaction cell during 30 min of visible-light irradiation using a thermocouple thermometer. As shown in Fig. S12, the culture dish was heated to 47.8 °C after 30 min of visible-light irradiation. The contribution of the increased temperature towards the NO<sub>x</sub> removal was further excluded by the temperature control experiment (Fig. S13, the detailed descriptions are provided in the supporting information).

In addition, the performance of C<sub>3</sub>N<sub>4.47</sub>H<sub>3.76</sub>O<sub>1.15</sub> was compared to other PCN-free catalysts (such as BiOCl, Bi<sub>2</sub>O<sub>2</sub>CO<sub>3</sub>, BiOBr, ZnFe<sub>2</sub>O<sub>4</sub>, SrTiO<sub>3</sub>, and commercial P25), and the results indicated C<sub>3</sub>N<sub>4.47</sub>H<sub>3.76</sub>O<sub>1.15</sub> had obvious advantages over the above classic PCN-free photocatalysts in the removal of NO and the inhibition of by-product NO<sub>2</sub> under visible-light irradiation (Fig. S14 and Table S6, the detailed descriptions are provided in the supporting information). The apparent quantum yield (AQY) of the representative samples was calculated (Table S7), and the results also indicated that the C<sub>3</sub>N<sub>4.47</sub>H<sub>3.76</sub>O<sub>1.15</sub> samples achieved the superior level of photooxidation for NO<sub>x</sub> removal among three catalysts (the details of AQY results were provided in the supporting information). In addition, C<sub>3</sub>N<sub>4.47</sub>H<sub>3.76</sub>O<sub>1.15</sub> was the most economical photocatalyst among the representative samples based on the lowest electric energy per order (E<sub>EO</sub>) value (Table S8).

After a single run, the products accumulated on the surface of PCN and C<sub>3</sub>N<sub>4.47</sub>H<sub>3.76</sub>O<sub>1.15</sub> were extracted using deionized water and examined using the ion chromatograph (IC) technique. The results reveal that 0.67 μmol of nitrate accumulated on PCN. Nitrite signals were not detected. On the surface of C<sub>3</sub>N<sub>4.47</sub>H<sub>3.76</sub>O<sub>1.15</sub>, 0.71 μmol of nitrate and 0.94 μmol of nitrite were detected (Fig. 2d). Fig. 2e shows that C<sub>3</sub>N<sub>4.47</sub>H<sub>3.76</sub>O<sub>1.15</sub> was stable over multiple cycles. The results indicate that hydroxylation of PCN can improve the photocatalytic activity of the sample toward NO<sub>x</sub> removal. The generation of nitrite on the surface of C<sub>3</sub>N<sub>4.47</sub>H<sub>3.76</sub>O<sub>1.15</sub> may indicate that the reaction pathways associated with NO-removal in the presence of hydroxylated PCN are different from those associated with PCN.

Then, spin-trap ESR tests and trapping experiments were performed to identify the critical photo-generated active species. As shown in Fig. S15, stronger signals for •O<sub>2</sub><sup>-</sup> and weaker signals for •OH were observed when pristine PCN was used for 5 min under visible-light irradiation. It has been previously reported that the formation of •OH radicals on pristine PCN can be attributed to the transformation of a part of •O<sub>2</sub><sup>-</sup> (in 5,5'-dimethyl-1-pyrroline-N-oxide, DMPO) when spin-trap ESR experiments are conducted in water [19,39]. During liquid-solid reactions, water molecules can be ionized to generate protons

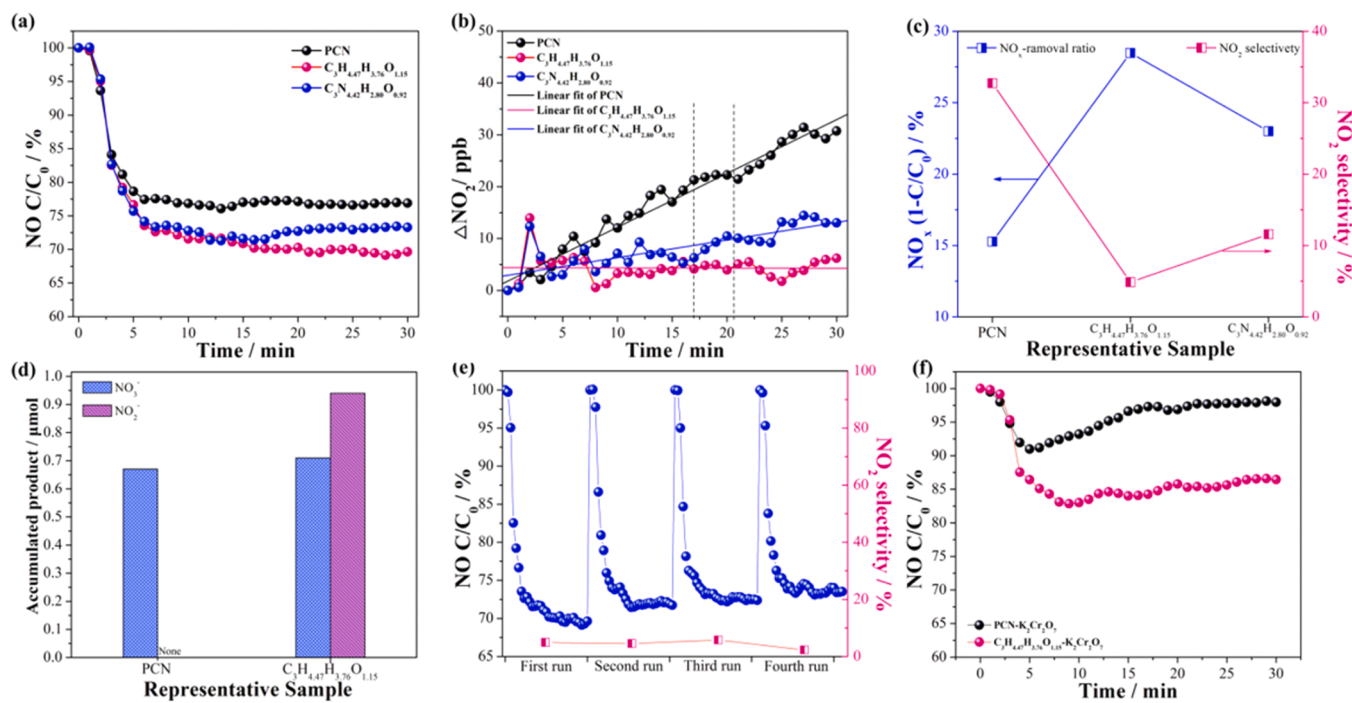


**Fig. 2.** (a) Photocatalytic activity evaluation of the representative samples towards NO removal under visible light irradiation, (b)  $\text{NO}_2$  generation, and (c)  $\text{NO}_x$ -removal ratios and  $\text{NO}_2$  selectivities recorded for the PCN,  $\text{C}_3\text{N}_{4.47}\text{H}_{3.76}\text{O}_{1.15}$ , and  $\text{C}_3\text{N}_{4.42}\text{H}_{2.80}\text{O}_{0.92}$  samples. (d) IC results of PCN and  $\text{C}_3\text{N}_{4.47}\text{H}_{3.76}\text{O}_{1.15}$ . (e) Cycling performance of  $\text{C}_3\text{N}_{4.47}\text{H}_{3.76}\text{O}_{1.15}$ . (f) Photogenerated-electron trapping experiments conducted with PCN and  $\text{C}_3\text{N}_{4.47}\text{H}_{3.76}\text{O}_{1.15}$ .

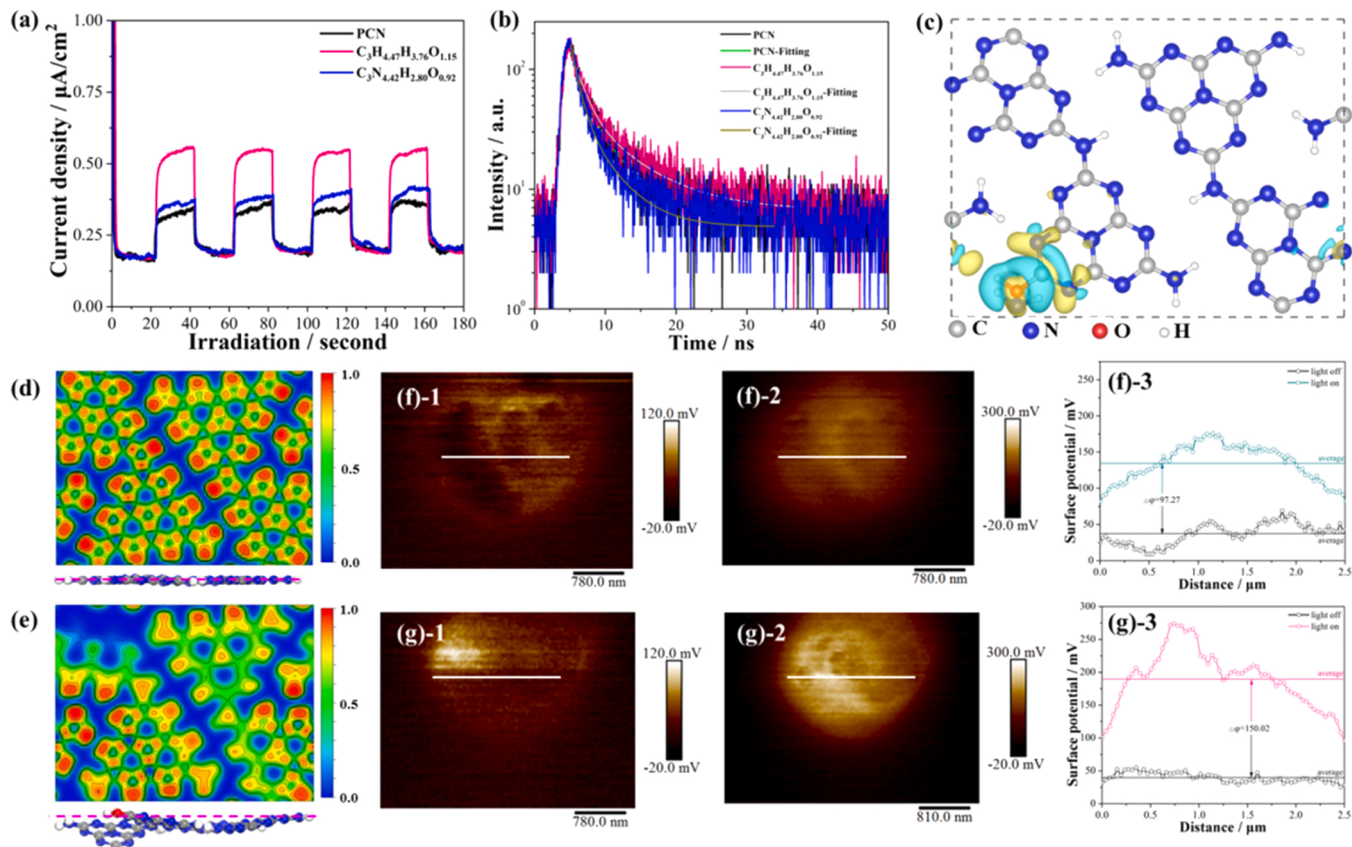


**Fig. 3.** (a) Transient photocurrent responses and (b) time-resolved fluorescence decay spectral profiles of PCN,  $\text{C}_3\text{N}_{4.47}\text{H}_{3.76}\text{O}_{1.15}$ , and  $\text{C}_3\text{N}_{4.42}\text{H}_{2.80}\text{O}_{0.92}$ . (c) EDD recorded for structure OH-introduced PCN. The ELF contours of PCN before (d) and after (e) the introduction of the structure OH units. KPFM characterizations of PCN (f) and  $\text{C}_3\text{N}_{4.47}\text{H}_{3.76}\text{O}_{1.15}$  (g) (surface potential in the dark: f-1 and g-1; surface potential under conditions of illumination: f-2 and g-2; surface potential curve: f-3 and g-3).

spontaneously. A proportion of  $\bullet\text{O}_2^-$  reacted with protons, leading to the generation of  $\bullet\text{OH}$  radicals via the  $\bullet\text{O}_2^- \rightarrow \text{H}_2\text{O}_2 \rightarrow \bullet\text{OH}$  route.<sup>39</sup> However, the  $\bullet\text{OH}$  trapping experiment shows that the contribution of  $\bullet\text{OH}$  to NO removal in the presence of pristine PCN can be ignored (Fig. S16). This suggests that few  $\bullet\text{OH}$  can be formed from  $\bullet\text{O}_2^-$  on the gas-solid interface of PCN in the gaseous phase reaction due to the dearth of a proton supplier (water vapor rarely ionizes to produce proton under ambient working conditions). In addition, the NO-removal ratio of PCN decreased from 23.2% to 2.0% following the introduction of  $\text{K}_2\text{Cr}_2\text{O}_7$  (Fig. 2f), indicating that photo-generated electrons were the dominant contributors to NO-removal (over pristine PCN). In contrast, the NO-removal ratio of  $\text{C}_3\text{N}_{4.47}\text{H}_{3.76}\text{O}_{1.15}$  remained at 13.5% following the introduction of  $\text{K}_2\text{Cr}_2\text{O}_7$  (Fig. 2f), suggesting that except for the photo-generated electrons, other active species participated in NO-removal.

### 3.3. The role of hydroxylation in photocatalytic activity enhancement

The photocatalytic  $\text{NO}_x$  removal reaction involves photon absorption, carrier separation, and  $\text{NO}_x$  surface catalytic oxidation. UV-vis diffuse reflectance spectroscopy of the samples (Fig. S17) suggests that surface-grafted OH groups reduce the intensity of absorption tails and structure-grafted OH groups slightly blue-shift the intrinsic absorption edges. Thus, it could be concluded that the optical absorbing ability did not play a role in the improved photocatalytic activity of the system.

Transient photocurrents, time-resolved fluorescence decay spectra, DFT calculation results, and KPFM were analyzed to evaluate the separation and migration behaviors of the photo-generated charges. Fig. 3a shows that the maximum current density is recorded for  $\text{C}_3\text{N}_{4.47}\text{H}_{3.76}\text{O}_{1.15}$ . The current density recorded for  $\text{C}_3\text{N}_{4.42}\text{H}_{2.80}\text{O}_{0.92}$  was slightly higher than that recorded for PCN. The time-resolved fluorescence decay spectral profiles with multi-exponential fitting are shown in Fig. 3b, and the respective kinetic parameters are listed in Table S9. The average lifetime of the photo-generated charge carriers were 4.14 ns, 6.21 ns, and 3.63 ns for PCN,  $\text{C}_3\text{N}_{4.47}\text{H}_{3.76}\text{O}_{1.15}$ , and  $\text{C}_3\text{N}_{4.42}\text{H}_{2.80}\text{O}_{0.92}$ , respectively. The results indicate the improvement of the electron-hole separation efficiency could be attributed to the introduction of the structure OH groups into the tri-s-triazine units. The OH groups grafted on the surface did not play a role. Based on this, the electron density differences (EDDs), Bader charge, and electronic localization function (ELF) were analyzed to further illustrate the change in the electron distribution following the introduction of the structure OH groups into the tri-s-triazine units. The EDDs results reveal that the charges were primarily depleted from the C atoms (blue areas) and accumulated at O and N atoms (yellow areas), as shown in Fig. 3c. The Bader charge analysis method was used to identify the perfect surface. The structural hydroxyl-grafted surface was also analyzed, and the results have been presented in Table S10. The results reveal that the total charges corresponding to the C atoms in the  $\text{C}_6\text{N}_7$  unit reduce 0.2 electrons following the introduction of OH. This helps in the subsequent oxidization of the grafted OH, resulting in the formation of  $\bullet\text{OH}$ . The electronic localization function (ELF) contours of the perfect PCN surface map show that the electron density is highly localized at the C and N sites (Fig. 3d). This is consistent with the characteristics of the covalent polymer. Meanwhile, the plane in which all the atoms are located is parallel to the (001) plane direction of PCN. The ELF map of the structural OH introduced into PCN shows that the O atom and neighboring C atom are surrounded by highly localized electron densities (Fig. 3e), indicating that a stable covalent bond is formed between the C and O atoms. In addition, compared with the pristine PCN (001) plane, the electron densities of the melon units no longer located in the original 2D plane following the introduction of the structural OH units. The twisting of the melon units can generate new 3D spatial polarized electric fields in which the separation efficiency of the carriers is improved because of spontaneous polarization [40,41]. For an in-depth understanding of the role of polarization, the surface potential (SP) of the representative

samples was studied by KPFM in the dark (SP1) and under light illumination (SP2). The difference in the surface potential ( $\Delta\varphi = \text{SP2}_{\text{average}} - \text{SP1}_{\text{average}}$ ) was subsequently calculated. As shown in Figs. 3f, g, and S18, the  $\Delta\varphi$  value corresponding to PCN,  $\text{C}_3\text{N}_{4.47}\text{H}_{3.76}\text{O}_{1.15}$ , and  $\text{C}_3\text{N}_{4.42}\text{H}_{2.80}\text{O}_{0.92}$  are 97.27, 150.02, and 78.04 mV, respectively. This further confirms that the spontaneous polarization process is the crucial factor for improving the separation efficiency of the photo-generated charge [40,42]. These above-mentioned results demonstrate that structure hydroxylation helps improve the separation efficiency of the carriers, resulting in the enhancement of photocatalytic activity. However, the roles of surface hydroxylation in photocatalytic-activity enhancement for  $\text{NO}_x$  removal, especially for  $\text{NO}_2$  inhibition, require further investigation.

The in-situ DRIFTS technique was used to monitor the surface species to identify the photocatalytic  $\text{NO}_x$  reaction pathways over PCN (following hydroxylation). A background spectrum was recorded after pretreating every sample using high-purity He during the in-situ DRIFTS measurements. After adsorption equilibrium was established, a visible light source was introduced to initiate the photoreaction processes. Fig. 4a shows the time-dependent DRIFTS images recorded during the photocatalytic oxidation of  $\text{NO}_x$  over the PCN sample. The band at  $829\text{ cm}^{-1}$  was assigned to the surface peroxy species, the intensity of which gradually decreased as the illumination time was increased. New absorption bands appeared at 920 (broad), 1047, and  $1600 - 1800\text{ cm}^{-1}$ , which were assigned to  $\text{NO}_2/\text{N}_2\text{O}_4$ , nitrate, and typical combination bands associated with NO and free nitrate, respectively [10,19,43,44]. The intensities gradually increased with the illumination time. The results indicate that NO can be oxidized to form toxic byproducts ( $\text{NO}_2/\text{N}_2\text{O}_4$ ) and end-products (nitrate) on the PCN surface.

Following this, the CI-NEB method was used to further elucidate the  $\text{NO}_x$ -removal pathways and search the transition states formed during the critical elementary reactions occurring on the PCN surface. The validity of the calculated transition state was verified by the uniqueness of imaginary frequency (f/i), as shown in Table S11. The initial states of the NO and  $\text{O}_2$  co-adsorption model ( $[\text{NO} + \text{O}_2]^*$ ) on the PCN surface were built, as shown in Fig. 4b (The possible adsorption positions of  $\text{O}_2$  and  $^*\text{O}$  on the PCN surface have been optimized and presented in the supporting information; Fig. S19 and Table S12). In  $^*[\text{NO} + \text{O}_2]$ , the distance between the N atom present in NO and the closest O atom in  $\text{O}_2$  ( $d_1$ ) was 1.91 Å. The band length of O-O in  $\text{O}_2$  was 1.26 Å. At the beginning of the photoreaction,  $\text{O}_2$  was activated and then dissociated into two O atoms to form the  $^*\text{NO}_2$  and  $^*\text{O}$  species on the PCN surface via the transition state TS1a (the O-O bond was elongated to 1.78 Å, and the  $d_1$  decreased from 1.91 to 1.27 Å). The results of energy calculation indicate that oxidation of NO to  $^*\text{NO}_2$  on the PCN surface (path 1) is endothermic (0.6 eV), and the activation barrier (activation energy,  $E_a$ ) was 1.46 eV. Subsequently, the formed  $^*\text{NO}_2$  is directly released as  $\text{NO}_2$  when 0.05 eV of energy is absorbed (path 2). Alternatively, it can be further oxidized by  $^*\text{O}$  to generate the  $^*\text{NO}_3^-$  structure via TS2a ( $E_a = 0.31\text{ eV}$ ; path 3). Following the release of  $\text{NO}_2$ , the remaining  $^*\text{O}$  can react with NO to generate  $^*\text{NO}_2$  (path 4) via TS3a. The energy barrier recorded for this path was 0.26 eV, as shown in Fig. 4c. The formed  $^*\text{NO}_2$  further dissociated from the surface of PCN to release  $\text{NO}_2$  by absorbing 0.01 eV (path 5). These facts suggest that the oxidation of NO prefers forming free  $\text{NO}_2$  (over  $^*\text{NO}_3^-$ ) on the PCN surface. Paths 1–5 were the primary paths involved in the reaction during the first 17 min of the photo-reaction (Fig. 2a–b). When the production rate (path 2 and path 5) and consumption rate (path 3) of  $\text{NO}_2$  were equal, a dynamic equilibrium was established (17–21 min; Fig. 2a–b).

In addition, the interaction between  $^*\text{NO}_3^-$  and NO should be considered because of the disproportionation reaction, which has often been overlooked. Thus, the reaction between  $^*\text{NO}_3^-$  and NO on the surface of PCN was examined, as shown in Fig. 4d. First of all, NO can react with  $^*\text{NO}_3^-$  to form  $^*\text{O}_2\text{NO-NO}$  (the distance between the N atom in NO and the closest O atom in  $^*\text{NO}_3^-$  ( $d_2$ ) decreased from 2.03 to 1.61 Å; the length of the N-O bond ( $d_3$ ) in  $^*\text{NO}_3^-$  increased from 1.29 to 1.47 Å.)

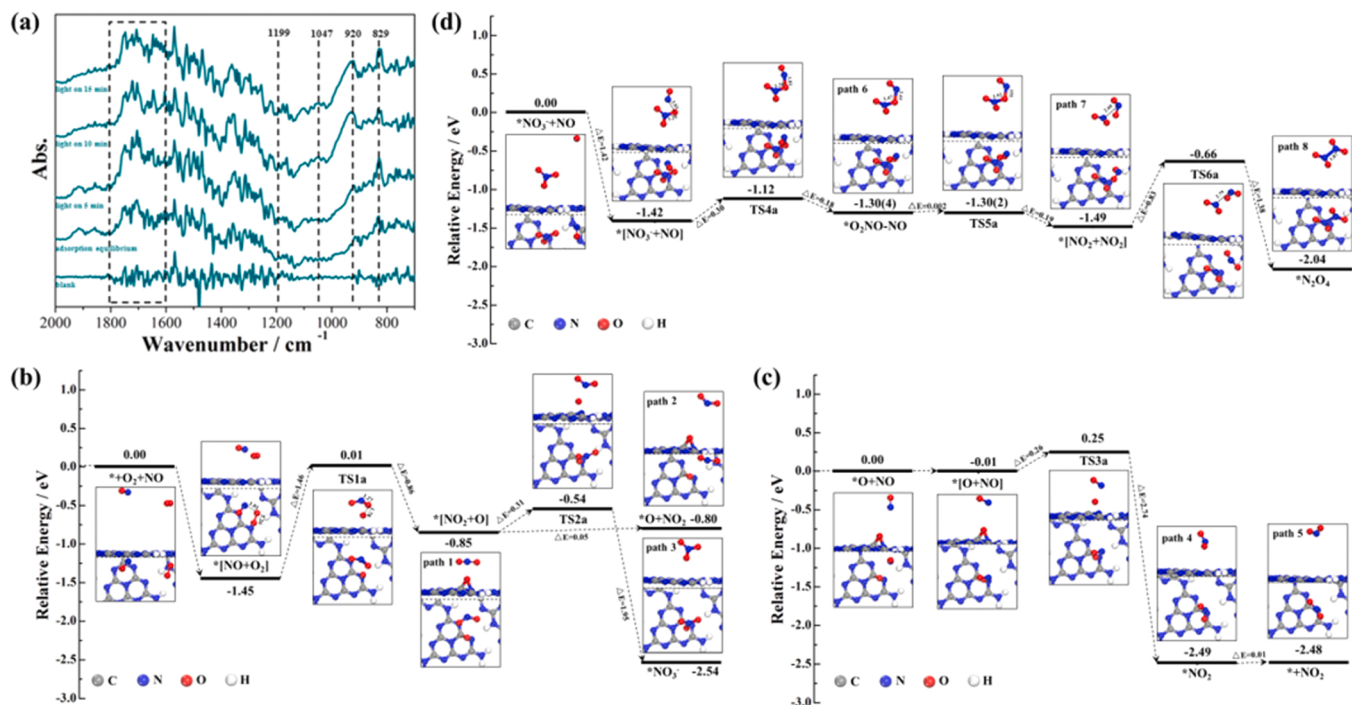


**Fig. 4.** (a) Time-dependent DRIFTS images recorded for the NO<sub>x</sub> photocatalytic oxidation process occurring on PCN. (b–d) Potential energy profiles recorded for the process of NO<sub>x</sub>-removal on the PCN surface. \*represents the catalyst surface, \*A and \* [A+B] represent the adsorption state and co-adsorption state of A and A+B on the catalyst surface, respectively.

via TS4a ( $d_2 = 1.81 \text{ \AA}$ ,  $d_3 = 1.38 \text{ \AA}$ ). The energy barrier was 0.30 eV (path 6). This process was endothermic (by 0.12 eV). Following this, NO captures the O atom in NO<sub>3</sub><sup>-</sup> to further form NO<sub>2</sub> (path 7) via the transition state TS5a (0.002 eV;  $d_2$  decreased from 1.61 to 1.55 Å;  $d_3$

increases from 1.47 to 1.52 Å). This process is exothermic by 0.19 eV. Finally, the surface-accumulated NO<sub>2</sub> can be further converted to N<sub>2</sub>O<sub>4</sub> (path 8) with an activation barrier (TS6a) of 0.83 eV. The NO<sub>2</sub> yield on PCN increased again when dynamic equilibrium became imbalanced

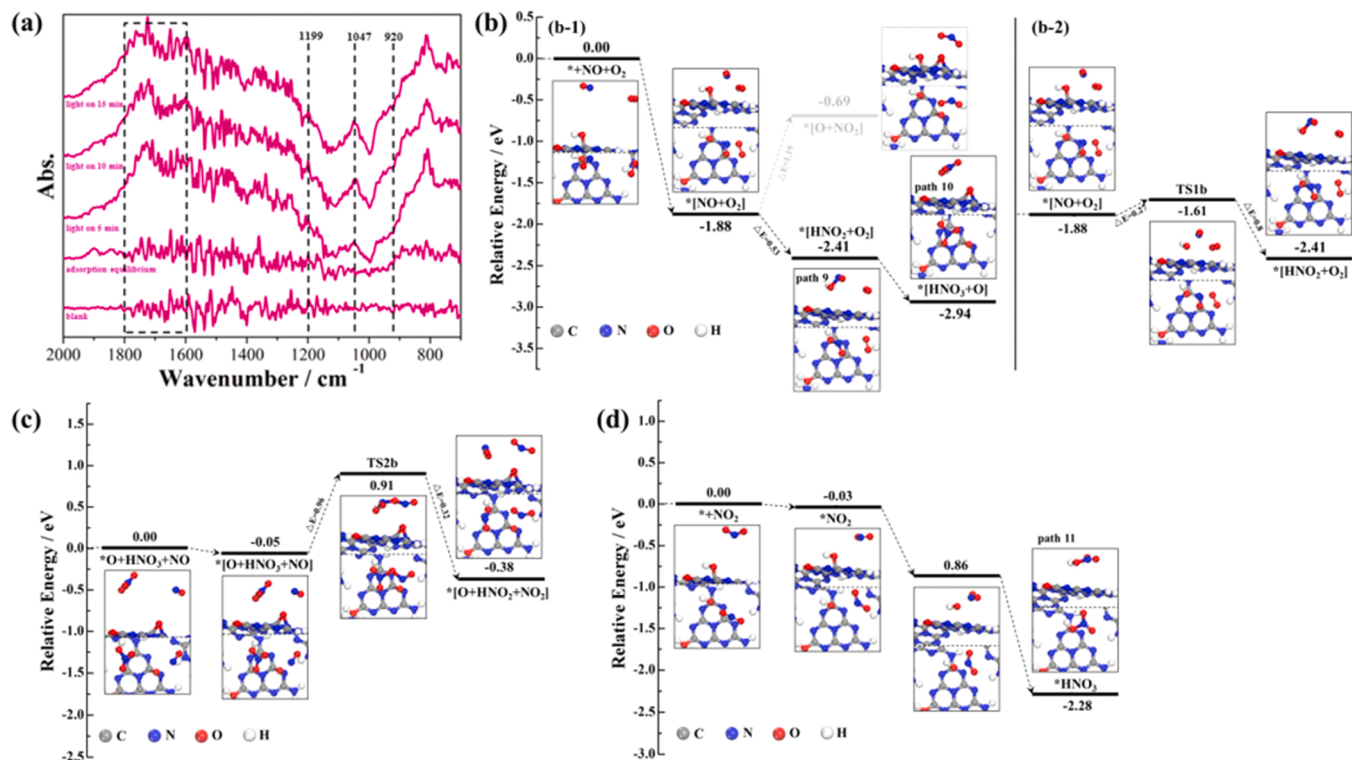


**Fig. 5.** (a) Time-dependent DRIFTS images recorded during the processes of NO<sub>x</sub> photocatalytic oxidation in the presence of C<sub>3</sub>N<sub>4.47</sub>H<sub>3.76</sub>O<sub>1.15</sub>. (b–d) Potential energy profiles recorded for the process of NO<sub>x</sub>-removal occurring on the C<sub>3</sub>N<sub>4.47</sub>H<sub>3.76</sub>O<sub>1.15</sub> surface. \*represents the catalyst surface, \*A and \* [A+B] represent the adsorption state and co-adsorption state of A and A+B on the catalyst surface, respectively.

(the process spanning the time range 21–30 min; Fig. 2a-b), and this could be attributed to the existence of paths 6–7. The appearance of the new peak in the range of 1600 – 1800 cm<sup>-1</sup> and at 920 cm<sup>-1</sup> (broad) can be attributed to pathways 6–8 (Fig. 4a).

Compared to the characteristic peaks of PCN (subjected to photoreaction processes), a new absorption band corresponding to nitrite appeared at 1199 cm<sup>-1</sup> is observed in the DRIFTS profile (Fig. 5a) [44, 45]. The peaks corresponding to nitrates and the combination band associated with NO and free nitrate present on the C<sub>3</sub>N<sub>4.47</sub>H<sub>3.76</sub>O<sub>1.15</sub> surface were more intense than those on the CN surface. Unexpectedly, no absorption band at approximately 920 cm<sup>-1</sup> (NO<sub>2</sub>/N<sub>2</sub>O<sub>4</sub>) was observed. The results indicate that NO can be oxidized to form nitrite and nitrate on the C<sub>3</sub>N<sub>4.47</sub>H<sub>3.76</sub>O<sub>1.15</sub> surface, while the formation of NO<sub>2</sub>/N<sub>2</sub>O<sub>4</sub> can be inhibited. The NO<sub>x</sub>-removal pathways and critical elementary reactions occurring in the presence of C<sub>3</sub>N<sub>4.47</sub>H<sub>3.76</sub>O<sub>1.15</sub> were studied to further understand the differences in the DRIFTS profiles recorded in the presence of PCN and C<sub>3</sub>N<sub>4.47</sub>H<sub>3.76</sub>O<sub>1.15</sub>. The initial states of the NO and O<sub>2</sub> co-adsorption model (\*[NO+O<sub>2</sub>]) on C<sub>3</sub>N<sub>4.47</sub>H<sub>3.76</sub>O<sub>1.15</sub> were built, as shown in Fig. 5b. In sharp contrast, it was observed that the NO unit present on the C<sub>3</sub>N<sub>4.47</sub>H<sub>3.76</sub>O<sub>1.15</sub> surface preferred reacting with the surface-grafted OH units, resulting in the generation of HNO<sub>2</sub> (path 9) via TS1b (E<sub>a</sub> = 0.28 eV). \*NO<sub>2</sub> (reaction energy,  $\Delta E$  = 1.19 eV) was not formed at the beginning of the photoreaction. These results agree well with the results obtained using the IC technique and FT-IR technique (Fig. S20). Compared to path 9, the path for NO oxidation associated with the structural hydroxyl group can be neglected because of thermodynamic disadvantage (Fig. S21). According to the redox rules, the formed HNO<sub>2</sub> cannot react with NO to release NO<sub>2</sub> but can be further oxidized by •O<sub>2</sub><sup>-</sup> to form HNO<sub>3</sub> (path 10). However, compared with path 7, NO cannot spontaneously react with HNO<sub>3</sub> to form NO<sub>2</sub> due to the presence of a high energy barrier (TS2b, E<sub>a</sub> = 0.91 eV, Fig. 5c). Although the surface \*O can oxidize NO to generate \*NO<sub>2</sub> (Fig. S22), the adjacent -OH group can spontaneously capture it to form \*HNO<sub>3</sub> (Fig. 5d, path 11). The single f/i value of TS1b and TS2b was listed in Table S11. The different reaction pathways associated with C<sub>3</sub>N<sub>4.47</sub>H<sub>3.76</sub>O<sub>1.15</sub> contribute to the observed inhibition of NO<sub>2</sub> formation. The extent of NO<sub>2</sub> emission realized during the photoreaction stage is lower under these conditions than that realized with the pristine PCN.

Based on the aforementioned chain of evidence, different reaction pathways in which NO<sub>x</sub> removal followed on the surface of PCN and C<sub>3</sub>N<sub>4.47</sub>H<sub>3.76</sub>O<sub>1.15</sub> are depicted in Fig. 6. Simply speaking, the NO

present on the PCN surface is oxidized by •O<sub>2</sub><sup>-</sup> to form \*NO<sub>2</sub> (path 1) which is directly released as NO<sub>2</sub> (path 2) or further oxidized by \*O to generate \*NO<sub>3</sub><sup>-</sup> (path 3). The remaining \*O reacts with NO to generate \*NO<sub>2</sub> (path 4) which further dissociates from the surface of PCN to release NO<sub>2</sub> through path 5. The formed \*NO<sub>3</sub><sup>-</sup> is not stable because of the disproportionation reaction with NO. The NO captures the O atom in \*NO<sub>3</sub><sup>-</sup> to further form NO<sub>2</sub> (path 6–7), leading to the increased NO<sub>2</sub> yield on PCN again. The surface-accumulated NO<sub>2</sub> is further converted to N<sub>2</sub>O<sub>4</sub> through path 8. In sharp contrast, it is observed that the NO present on the C<sub>3</sub>N<sub>4.47</sub>H<sub>3.76</sub>O<sub>1.15</sub> surface preferred reacting with the surface-grafted OH units rather than •O<sub>2</sub><sup>-</sup>, resulting in the generation of HNO<sub>2</sub> (path 9). According to the redox rules, the formed HNO<sub>2</sub> cannot react with NO to release NO<sub>2</sub> but can be further oxidized by •O<sub>2</sub><sup>-</sup> to form HNO<sub>3</sub> (path 10). However, compared with path 7, NO cannot spontaneously react with HNO<sub>3</sub> to form NO<sub>2</sub> due to the presence of a high energy barrier. Although the surface \*O can oxidize NO to generate \*NO<sub>2</sub>, the adjacent -OH group spontaneously captures it to form \*HNO<sub>3</sub> to avoid NO<sub>2</sub> emission (path 11).

#### 4. Conclusion

In summary, the results reveal that the efficient removal of dilute-NO and the effective inhibition of the process of formation of NO<sub>2</sub> can be achieved simultaneously using a hydroxylated PCN characterized by grafted hydroxyls that play multiple roles during the processes. The optimal sample, C<sub>3</sub>N<sub>4.47</sub>H<sub>3.76</sub>O<sub>1.15</sub>, exhibited a NO<sub>x</sub>-removal ratio that was 2 times higher than that exhibited by pristine PCN. This sample could be used to realize the complete inhibition of NO<sub>2</sub> formation. The grafted structural hydroxyl units can twist the melon unit, which generates new 3D spatial polarized electric fields to improve the separation efficiency of the carriers. The results obtained using the in-situ DRIFTS and DFT techniques revealed that the inhibition in NO<sub>2</sub> formation and emission during the photoreaction stage was induced by the grafted surface hydroxyl units. These factors help achieve the complete photocatalytic-oxidation-based removal of NO<sub>x</sub>. The results reported herein provide a new perspective (at a molecular level) to recognize the multiplicity of the grafted hydroxyls associated with the photocatalytic oxidation of NO<sub>x</sub> on the surface of PCN.

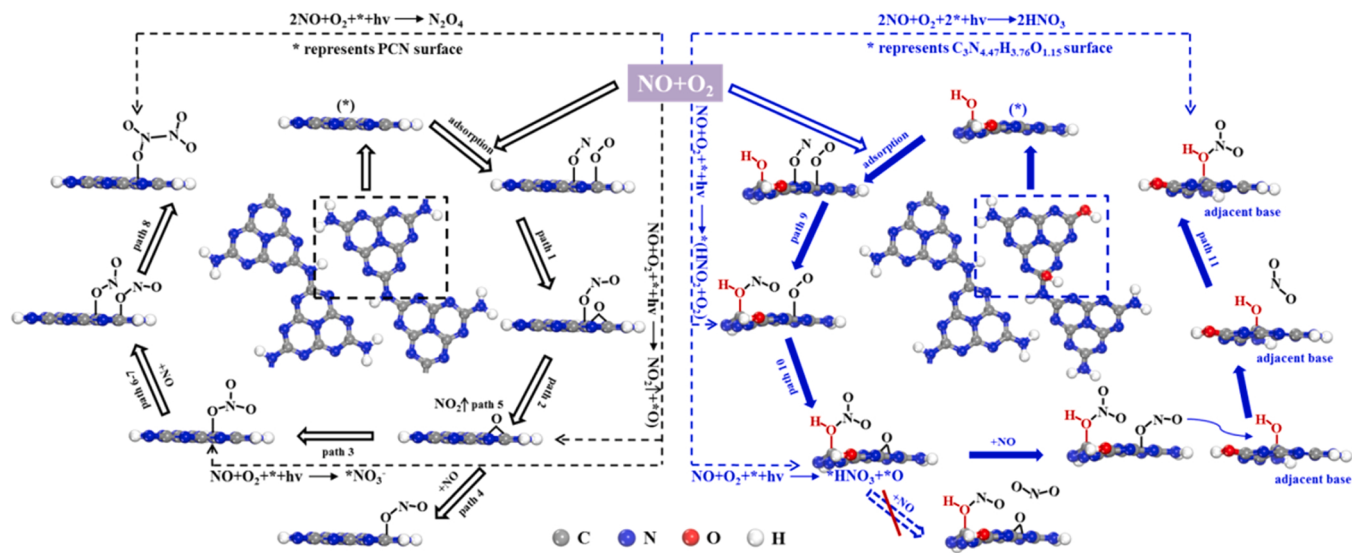


**Fig. 6.** Schematic representation of the proposed reaction pathways associated with the process of NO<sub>x</sub> photocatalytic oxidation on the surface of PCN and C<sub>3</sub>N<sub>4.47</sub>H<sub>3.76</sub>O<sub>1.15</sub>. The route indicated with black arrows: elementary steps for the formation of NO<sub>3</sub><sup>-</sup>, NO<sub>2</sub>, and N<sub>2</sub>O<sub>4</sub> on the PCN (100) plane. The route indicated with blue arrows: elementary steps for the formation of HNO<sub>2</sub> and HNO<sub>3</sub> on the C<sub>3</sub>N<sub>4.47</sub>H<sub>3.76</sub>O<sub>1.15</sub> (100) plane.

## CRediT authorship contribution statement

**Zhenyu Wang, QiuHua Wei:** Contributed equally to this work.  
**Zhenyu Wang, QiuHua Wei:** Conceptualization, Investigation, Writing – original draft.  
**Ning Zhang:** Experimental operation.  
**Xianjin Shi:** Data curation, Validation.  
**Meijuan Chen:** Writing – review & editing.  
**Yu Huang, Junji Cao:** Resources, Supervision.  
**Haiwei Li:** Writing – review & editing.  
**Wingkei Ho:** Writing – polishing.  
**ShunCheng Lee:** Supervision.

## Declaration of Competing Interest

The authors declare that they have no known competing financial interests or personal relationships that could have appeared to influence the work reported in this paper.

## Data availability

No data was used for the research described in the article.

## Acknowledgment

This research was financially supported by the Strategic Priority Research Program of the Chinese Academy of Sciences (No. XDA23010300 and XDA23010301), the Plan for "National Youth Talents" of the Organization Department of the Central Committee. Zhenyu Wang was supported by the China National Postdoctoral Program for Innovative Talents (No. BX20200331), the China Postdoctoral Science Foundation (No. 2020M673521), and the Special Research Assistant Grant Program of the Chinese Academy of Sciences.

## Supporting Information

Performance comparison of PCN and PCN-based photocatalysts for NO<sub>x</sub>-removal (Table S1), visible light photocatalytic activities of PCN subjected to alkaline hydrothermal treatment processes (Fig. S1, Table S2), schematic flow diagram of the experimental set-up system (Fig. S2), FT-IR spectral profiles (Fig. S3), element contents (Table S3), modeling process of representative samples (Figs. S4, S7–S10 and Table S4), O 1 s XPS spectrum for PCN (Fig. S5), reaction scheme for the hydrolysis of PCN (Fig. S6), SEM images (Fig. S11), linear regression method followed for the production of NO<sub>2</sub> (Table S5), temperature variation of the photocatalyst surface during 30 min of visible-light irradiation (Fig. S12), catalytic activity evaluation under different temperature (Fig. S13), photocatalytic activity evaluation of the PCN-free photocatalysts (Fig. S14 and Table S6), the calculated values of AQY (Table S7) and E<sub>PO</sub> (Table S8), DMPO spin-trap ESR spectra (Fig. S15), trapping experiments (Fig. S16), UV-vis absorption spectral profiles (Fig. S17), fluorescence lifetime (Table S9), atomic bader charges (Table S10), KPFM characterization results (Fig. S18), calculated imaginary frequency (Table S11), possible adsorption positions corresponding to O<sub>2</sub> and \*O (Fig. S19 and Table S12), FT-IR spectra after single reaction and washing (Fig. S20), potential energy profiles for NO-removal at the structural OH (Fig. S21) and \*O sites (Fig. S22).

## Appendix A. Supporting information

Supplementary data associated with this article can be found in the online version at doi:10.1016/j.apcatb.2023.122582.

## References

- [1] Z. An, R.J. Huang, R. Zhang, X. Tie, G. Li, J. Cao, W. Zhou, Z. Shi, Y. Han, Z. Gu, Y. Ji, Severe haze in northern China: A synergy of anthropogenic emissions and atmospheric processes, Proc. Natl. Acad. Sci. U. S. A. 116 (2019) 8657–8666, <https://doi.org/10.1073/pnas.1900125116>.
- [2] T. Wang, L. Xue, P. Brimblecombe, Y.F. Lam, L. Li, L. Zhang, Ozone pollution in China: A review of concentrations, meteorological influences, chemical precursors, and effects, Sci. Total. Environ. 575 (2017) 1582–1596, <https://doi.org/10.1016/j.scitotenv.2016.10.081>.
- [3] P. Granger, V.I. Parvulescu, Catalytic NO<sub>x</sub> abatement systems for mobile sources: from three-way to lean burn after-treatment technologies, Chem. Rev. 111 (2011) 3155–3207, <https://doi.org/10.1021/cr100168g>.
- [4] J.J. Cao, Y. Huang, Q. Zhang, Ambient air purification by nanotechnologies: from theory to application, Catalysts 11 (2021), <https://doi.org/10.3390/catal11111276>. ARTN 1276.
- [5] Y. Huang, J. Zhang, Z.Y. Wang, Y. Liu, P.G. Wang, J.J. Cao, W.K. Ho, g-C<sub>3</sub>N<sub>4</sub>/TiO<sub>2</sub> composite film in the fabrication of a photocatalytic air-purifying pavements, Sol. Rrl 4 (2020), <https://doi.org/10.1002/solr.202000170>. ARTN 2000170.
- [6] H. Shang, M. Li, H. Li, S. Huang, C. Mao, Z. Ai, L. Zhang, Oxygen Vacancies Promoted the Selective Photocatalytic Removal of NO with Blue TiO<sub>2</sub> via Simultaneous Molecular Oxygen Activation and Photogenerated Hole Annihilation, Environ. Sci. Technol. 53 (2019) 6444–6453, <https://doi.org/10.1021/acs.est.8b07322>.
- [7] S. Xiao, D. Zhang, D. Pan, W. Zhu, P. Liu, Y. Cai, G. Li, H. Li, A chloroplast structured photocatalyst enabled by microwave synthesis, Nat. Commun. 10 (2019) 1570, <https://doi.org/10.1038/s41467-019-10509-y>.
- [8] H. Chen, C.E. Nanayakkara, V.H. Grassian, Titanium dioxide photocatalysis in atmospheric chemistry, Chem. Rev. 112 (2012) 5919–5948, <https://doi.org/10.1021/cr3002092>.
- [9] Y. Nosaka, A.Y. Nosaka, Generation and detection of reactive oxygen species in photocatalysis, Chem. Rev. 117 (2017) 11302–11336, <https://doi.org/10.1021/acscchemrev.7b00161>.
- [10] H. Li, H. Shang, X. Cao, Z. Yang, Z. Ai, L. Zhang, Oxygen Vacancies Mediated Complete Visible Light NO Oxidation via Side-On Bridging Superoxide Radicals, Environ. Sci. Technol. 52 (2018) 8659–8665, <https://doi.org/10.1021/acs.est.8b01849>.
- [11] X. Wang, K. Maeda, A. Thomas, K. Takanabe, G. Xin, J.M. Carlsson, K. Domen, M. Antonietti, A metal-free polymeric photocatalyst for hydrogen production from water under visible light, Nat. Mater. 8 (2009) 76–80, <https://doi.org/10.1038/nmat2317>.
- [12] X. Zhang, X. Xie, H. Wang, J. Zhang, B. Pan, Y. Xie, Enhanced photoresponsive ultrathin graphitic-phase C<sub>3</sub>N<sub>4</sub> nanosheets for bioimaging, J. Am. Chem. Soc. 135 (2013) 18–21, <https://doi.org/10.1021/ja308249k>.
- [13] W.J. Ong, L.L. Tan, Y.H. Ng, S.T. Yong, S.P. Chai, Graphitic Carbon Nitride (g-C<sub>3</sub>N<sub>4</sub>)-Based Photocatalysts for Artificial Photosynthesis and Environmental Remediation: Are We a Step Closer To Achieving Sustainability, Chem. Rev. 116 (2016) 7159–7329, <https://doi.org/10.1021/acs.chemrev.6b00075>.
- [14] C. Chu, Q. Zhu, Z. Pan, S. Gupta, D. Huang, Y. Du, S. Weon, Y. Wu, C. Muhich, E. Stavitski, K. Domen, J.H. Kim, Spatially separating redox centers on 2D carbon nitride with cobalt single atom for photocatalytic H<sub>2</sub>O<sub>2</sub> production, Proc. Natl. Acad. Sci. U. S. A. 117 (2020) 6376–6382, <https://doi.org/10.1073/pnas.1913403117>.
- [15] C. Huang, Y. Wen, J. Ma, D. Dong, Y. Shen, S. Liu, H. Ma, Y. Zhang, Unraveling fundamental active units in carbon nitride for photocatalytic oxidation reactions, Nat. Commun. 12 (2021) 320, <https://doi.org/10.1038/s41467-020-20521-5>.
- [16] T. Sano, S. Tsutsui, K. Koike, T. Hirakawa, Y. Teramoto, N. Negishi, K. Takeuchi, Activation of graphitic carbon nitride (g-C<sub>3</sub>N<sub>4</sub>) by alkaline hydrothermal treatment for photocatalytic NO oxidation in gas phase, J. Mater. Chem. A 1 (2013) 6489–6496, <https://doi.org/10.1039/c3ta10472a>.
- [17] T. Xiong, W.L. Cen, Y.X. Zhang, F. Dong, Bridging the g-C<sub>3</sub>N<sub>4</sub> interlayers for enhanced photocatalysis, ACS Catal. 6 (2016) 2462–2472, <https://doi.org/10.1021/acscatal.5b02922>.
- [18] Z.Y. Wang, Y. Huang, W.K. Ho, J.J. Cao, Z.X. Shen, S.C. Lee, Fabrication of Bi<sub>2</sub>O<sub>2</sub>CO<sub>3</sub>/g-C<sub>3</sub>N<sub>4</sub> heterojunctions for efficiently photocatalytic NO in air removal: In-situ self-sacrificial synthesis, characterizations and mechanistic study, Appl. Catal. B-Environ. 199 (2016) 123–133, <https://doi.org/10.1016/j.apcatb.2016.06.027>.
- [19] Z. Wang, Y. Huang, M. Chen, X. Shi, Y. Zhang, J. Cao, W. Ho, S.C. Lee, Roles of N-Vacancies over Porous g-C<sub>3</sub>N<sub>4</sub> Microtubes during Photocatalytic NO<sub>x</sub> Removal, ACS Appl. Mater. Interfaces 11 (2019) 10651–10662, <https://doi.org/10.1021/acsami.8b21987>.
- [20] M.M. Montemore, M.A. van Spronsen, R.J. Madix, C.M. Friend, O<sub>2</sub> activation by metal surfaces: implications for bonding and reactivity on heterogeneous catalysts, Chem. Rev. 118 (2018) 2816–2862, <https://doi.org/10.1021/acs.chemrev.7b00217>.
- [21] H. Li, H. Shang, Y. Li, X. Cao, Z. Yang, Z. Ai, L. Zhang, Interfacial charging-decharging strategy for efficient and selective aerobic NO oxidation on oxygen vacancy, Environ. Sci. Technol. 53 (2019) 6964–6971.
- [22] C. Liu, Q.X. Ma, H. He, G.Z. He, J.Z. Ma, Y.C. Liu, Y. Wu, Structure-activity relationship of surface hydroxyl groups during NO<sub>2</sub> adsorption and transformation on TiO<sub>2</sub> nanoparticles, Environ. Sci. -Nano 4 (2017) 2388–2394, <https://doi.org/10.1039/c7en00920h>.
- [23] T. Kako, X.G. Meng, J.H. Ye, Enhancement of photocatalytic activity for WO<sub>3</sub> by simple NaOH loading, Appl. Catal. A-Gen. 488 (2014) 183–188, <https://doi.org/10.1016/j.apcata.2014.09.046>.
- [24] S. Ouyang, H. Tong, N. Umezawa, J. Cao, P. Li, Y. Bi, Y. Zhang, J. Ye, Surface-alkalinization-induced enhancement of photocatalytic H<sub>2</sub> evolution over SrTiO<sub>3</sub>-based photocatalysts, J. Am. Chem. Soc. 134 (2012) 1974–1977, <https://doi.org/10.1021/ja210610h>.
- [25] Y. Li, S. Ouyang, H. Xu, X. Wang, Y. Bi, Y. Zhang, J. Ye, Constructing Solid-Gas-Interfacial Fenton Reaction over Alkalized-C<sub>3</sub>N<sub>4</sub> Photocatalyst To Achieve

Apparent Quantum Yield of 49% at 420 nm, *J. Am. Chem. Soc.* 138 (2016) 13289–13297, <https://doi.org/10.1021/jacs.6b07272>.

[26] Y. Li, H. Xu, S. Ouyang, D. Lu, X. Wang, D. Wang, J. Ye, In situ surface alkalinized g-C<sub>3</sub>N<sub>4</sub> toward enhancement of photocatalytic H<sub>2</sub> evolution under visible-light irradiation, *J. Mater. Chem. A* 4 (2016) 2943–2950, <https://doi.org/10.1039/c5ta05128b>.

[27] N. Zhang, X. Li, H. Ye, S. Chen, H. Ju, D. Liu, Y. Lin, W. Ye, C. Wang, Q. Xu, J. Zhu, L. Song, J. Jiang, Y. Xiong, Oxide Defect Engineering Enables to Couple Solar Energy into Oxygen Activation, *J. Am. Chem. Soc.* 138 (2016) 8928–8935, <https://doi.org/10.1021/jacs.6b04629>.

[28] H. Nie, M. Ou, Q. Zhong, S. Zhang, L. Yu, Efficient visible-light photocatalytic oxidation of gaseous NO with graphitic carbon nitride (g-C<sub>3</sub>N<sub>4</sub>) activated by the alkaline hydrothermal treatment and mechanism analysis, *J. Hazard. Mater.* 300 (2015) 598–606, <https://doi.org/10.1016/j.jhazmat.2015.07.066>.

[29] Z.Y. Gu, Z.T. Cui, Z.J. Wang, K.S. Qin, Y. Asakura, T. Hasegawa, S. Tsukuda, K. Hongo, R. Maezono, S. Yin, Carbon vacancies and hydroxyls in graphitic carbon nitride: Promoted photocatalytic NO removal activity and mechanism (ARTN), *Appl. Catal. B-Environ.* 279 (2020), 119376, <https://doi.org/10.1016/j.apcatb.2020.119376>.

[30] J.P. Perdew, K. Burke, M. Ernzerhof, Generalized gradient approximation made simple, *Phys. Rev. Lett.* 77 (1996) 3865–3868, <https://doi.org/10.1103/PhysRevLett.77.3865>.

[31] G. Kresse, J. Furthmüller, Efficient iterative schemes for ab initio total-energy calculations using a plane-wave basis set, *Phys. Rev. B Condens. Matter* 54 (1996) 11169–11186, <https://doi.org/10.1103/physrevb.54.11169>.

[32] G. Kresse, D. Joubert, From ultrasoft pseudopotentials to the projector augmented-wave method, *Phys. Rev. B* 59 (1999) 1758–1775, <https://doi.org/10.1103/PhysRevB.59.1758>.

[33] G. Henkelman, A. Arnaldsson, H. Jonsson, A fast and robust algorithm for Bader decomposition of charge density, *Comp. Mater. Sci.* 36 (2006) 354–360, <https://doi.org/10.1016/j.commatsci.2005.04.010>.

[34] G. Henkelman, B.P. Uberuaga, H. Jonsson, A climbing image nudged elastic band method for finding saddle points and minimum energy paths, *J. Chem. Phys.* 113 (2000) 9901–9904. Pii [S0021-9606(00)71246-3] 10.1063/1.1329672.

[35] X.L. Wang, W.Q. Fang, H.F. Wang, H. Zhang, H. Zhao, Y. Yao, H.G. Yang, Surface hydrogen bonding can enhance photocatalytic H<sub>2</sub> evolution efficiency, *J. Mater. Chem. A* 1 (2013), <https://doi.org/10.1039/c3ta13328a>.

[36] Y. Li, Y. Wang, C.L. Dong, Y.C. Huang, J. Chen, Z. Zhang, F. Meng, Q. Zhang, Y. Huangfu, D. Zhao, L. Gu, S. Shen, Single-atom nickel terminating sp<sup>2</sup> and sp<sup>3</sup> nitride in polymeric carbon nitride for visible-light photocatalytic overall water splitting, *Chem. Sci.* 12 (2021) 3633–3643, <https://doi.org/10.1039/d0sc07093a>.

[37] H. Yu, R. Shi, Y. Zhao, T. Bian, Y. Zhao, C. Zhou, G.I.N. Waterhouse, L.Z. Wu, C. H. Tung, T. Zhang, Alkali-assisted synthesis of nitrogen deficient graphitic carbon nitride with tunable band structures for efficient visible-light-driven hydrogen evolution, *Adv. Mater.* 29 (2017), <https://doi.org/10.1002/adma.201605148>.

[38] Z.Y. Wang, Y. Huang, L. Chen, M.J. Chen, J.J. Cao, W.K. Ho, S.C. Lee, In situ g-C<sub>3</sub>N<sub>4</sub> self-sacrificial synthesis of a g-C<sub>3</sub>N<sub>4</sub>/LaCO<sub>3</sub>OH heterostructure with strong interfacial charge transfer and separation for photocatalytic NO removal, *J. Mater. Chem. A* 6 (2018) 972–981, <https://doi.org/10.1039/c7ta09132j>.

[39] W. Cui, J. Li, F. Dong, Y. Sun, G. Jiang, W. Cen, S.C. Lee, Z. Wu, Highly Efficient Performance and Conversion Pathway of Photocatalytic NO Oxidation on SrO-Clusters@Amorphous Carbon Nitride, *Environ. Sci. Technol.* 51 (2017) 10682–10690, <https://doi.org/10.1021/acs.est.7b00974>.

[40] L. Liu, H. Huang, Z. Chen, H. Yu, K. Wang, J. Huang, H. Yu, Y. Zhang, Synergistic polarization engineering on bulk and surface for boosting CO<sub>2</sub> photoreduction, in: *Angew. Chem. Int. Ed. Engl.*, 60, 2021, pp. 18303–18308, <https://doi.org/10.1002/anie.202106310>.

[41] S.X. Yu, J.Y. Li, Y.H. Zhang, M. Li, F. Dong, T.R. Zhang, H.W. Huang, Local spatial charge separation and proton activation induced by surface hydroxylation promoting photocatalytic hydrogen evolution of polymeric carbon nitride, *Nano Energy* 50 (2018) 383–392, <https://doi.org/10.1016/j.nanoen.2018.05.053>.

[42] S. Wang, Y. Gao, S. Miao, T. Liu, L. Mu, R. Li, F. Fan, C. Li, Positioning the water oxidation reaction sites in plasmonic photocatalysts, *J. Am. Chem. Soc.* 139 (2017) 11771–11778, <https://doi.org/10.1021/jacs.7b04470>.

[43] H. Wang, W.J. He, X.A. Dong, H.Q. Wang, F. Dong, In situ FT-IR investigation on the reaction mechanism of visible light photocatalytic NO oxidation with defective g-C<sub>3</sub>N<sub>4</sub>, *Sci. Bull.* 63 (2018) 117–125, <https://doi.org/10.1016/j.scib.2017.12.013>.

[44] J.Y. Li, X.A. Dong, Y.J. Sun, G.M. Jiang, Y.H. Chu, S.C. Lee, F. Dong, Tailoring the rate-determining step in photocatalysis via localized excess electrons for efficient and safe air cleaning, *Appl. Catal. B-Environ.* 239 (2018) 187–195, <https://doi.org/10.1016/j.apcatb.2018.08.019>.

[45] J.C.S. Wu, Y.T. Cheng, In situ FTIR study of photocatalytic NO reaction on photocatalysts under UV irradiation, *J. Catal.* 237 (2006) 393–404, <https://doi.org/10.1016/j.jcat.2005.11.023>.